Thickness-Dependent Nonlinear Electrical Conductivity of Few-Layer Muscovite Mica

Ankit Arora,[1,2] Kolla Lakshmi Ganapathi,[2] Tejendra Dixit,[3] Muralidhar Miryala,[4] Murakami Masato,[4] M.S. Ramachandra Rao,[2,*] and Ananth Krishnan[1,†]

[1] *Department of Electrical Engineering, Centre for NEMS and Nanophotonics (CNNP), Indian Institute of Technology Madras, Chennai 600036, India*

[2] *Department of Physics, Quantum Centres in Diamond and Emergent Materials (QuCenDiEM) Group, Nano Functional Materials Technology Centre and Materials Science Research Centre, Indian Institute of Technology Madras, Chennai 600036, India*

[3] *Department of Electronics and Communication Engineering, Indian Institute of Information Technology Design and Manufacturing, Kancheepuram, Chennai 600127, India*

[4] *Superconducting Material Laboratory, Graduate School of Science and Engineering, Shibaura Institute of Technology, Tokyo 135-8546, Japan*

(Received 10 April 2022; accepted 3 June 2022; published 23 June 2022)

We report on the direct current (dc) current-voltage (I-V) characteristics of few-layer muscovite mica (MuM) flakes exfoliated and transferred onto SiO_2/Si substrate, under different substrate dc bias voltages. Contrary to usual observations in conventional two-dimensional systems, we observe an increase in the in-plane electrical conductivity with a reducing thickness of MuM flakes. At a given voltage, the electrical conductivity of approximately five-layered MuM flake (T_3) is 3 orders of magnitude larger than that in approximately ten-layered MuM flake (T_2). The I-V characteristics are used to analyze the mechanism of conduction. The model-based analysis reveals the hopping-conduction mechanism to be dominant as compared to the Poole-Frenkel effect. The thickness-dependent work function is measured using Kelvin probe force microscopy for a MuM flake on Si substrate. Assuming that the measured work function is correlated with the Fermi level, we report an upward movement of the Fermi level, toward the conduction band with the reducing thickness of MuM flakes, indicating an increase in the conduction-band carrier density. The observed increase in conductivity in T_3 when compared to T_2 may be attributed to surface doping due to the increased contribution from K^+ ions and lattice relaxation. Our results show that there is a possibility of using few-layer mica as a wide-band-gap semiconductor and that it can open up different avenues for two-dimensional electronic devices.

DOI: 10.1103/PhysRevApplied.17.064042

I. INTRODUCTION

Due to their intriguing properties, two-dimensional (2D) van der Waals (vdW) materials are an emerging class of materials for next-generation electronic devices [1,2]. Most of these materials are, however, not stable in stringent chemical and physical conditions [3], thereby limiting their applications in electronics for harsh environments. Muscovite mica (MuM) is a naturally occurring layered vdW aluminosilicate commonly used as an electrical insulator and is known for its exceptional chemical and physical stability [4,5]. It has a complex structure consisting of an octahedral layer sandwiched between two tetrahedral layers as shown in Fig. 1, with a monoclinic unit cell ($a = 5.19$ Å, $b = 8.99$ Å, $c = 20.14$ Å, and $\beta = 96°$) [6]. The tetrahedral layer consists of a pseudohexagonal arrangement of SiO_4 tetrahedra, whereas the octahedral layer consists of an octahedron with Al^{3+} at the center. On average, one fourth of the tetrahedra have Si^{4+} randomly substituted by Al^{3+} and every third octahedron has a vacancy at the center. This excess negative charge due to tetrahedral trivalent substitution and octahedral vacancy is compensated by the interlayer cation K^+ ions which electrostatically hold the three-layered MuM stack together [5,6]. Due to electrostatic and packing constraints, these K^+ ions are situated at the center of the hexagon and interact electrostatically with six oxygen atoms on either

*msrrao@iitm.ac.in
†ananthk@iitm.ac.in

Published by the American Physical Society under the terms of the Creative Commons Attribution 4.0 International license. Further distribution of this work must maintain attribution to the author(s) and the published article's title, journal citation, and DOI.

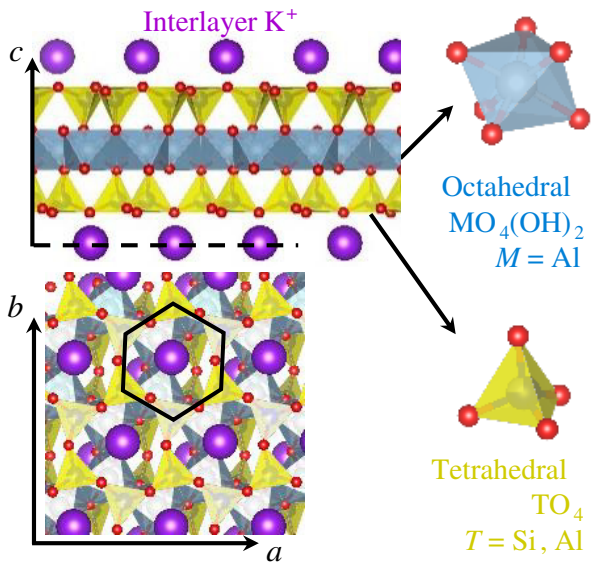

FIG. 1. A schematic of the crystal structure of the MuM monolayer along the indicated crystallographic directions, consisting of an octahedral layer (shown in blue) sandwiched between two tetrahedral layers (shown in yellow) with interlayer potassium ions (shown as magenta spheres) to maintain the charge neutrality.

side [5]. Weak bonding between the K^+ layer and the aluminosilicate layer gives mica its cleavage property. However, due to the charged nature of the layers, MuM has a cleavage energy of approximately 90 meV/Å^{-2} [7], which is almost 3 times that of conventional 2D materials such as graphene, transition-metal dichalcogenides, and hexagonal boron nitride [8].

With the rise of graphene and 2D vdW semiconductors, MuM has attracted attention as an ultraflat 2D substrate [9]. Exfoliated few-layer MuM has been demonstrated as a substrate for applications such as flexible electronics [10–12], vdW heteroepitaxy [13,14], multifunctional 2D electronics [14–17], memory devices [18–21], and as a layered gate dielectric for transistors [22,23]. MuM has been reported as an interesting substrate for graphene, with unique properties [24–27]. Recently, MuM has also been demonstrated as an atomically thin proton-conducting membrane [28].

The investigation of the electrical properties of MuM has a history of almost a century [29] and several mechanisms have been proposed to explain its electrical conduction [5,30–34]. However, none of the proposed models has been able to explain coherently all the experimental observations of MuM [5,33]. In almost all the studies reported so far, conduction across the layers has been measured, where the device architecture with closely placed electrodes has resulted in tunneling as a dominant current component and has made it difficult to extract the material-related information. Further, the electronic properties of monolayer and few-layer MuM are not well understood and there are not many reports on the thickness-dependent effects on the electronic properties of MuM [35].

In the present work, we report on the thickness-dependent in-plane electrical conductivity of few-layer MuM flakes. MuM flakes are mechanically exfoliated on SiO_2/Si substrates and the contact electrodes are defined as being approximately 1 μm apart, to avoid any tunneling phenomena. It is observed that the current in few-layer MuM ($\leq$20 nm) devices is flake-thickness dependent and that, at a given voltage, it is 3 orders of magnitude larger in approximately 10-nm-thick MuM when compared to that in approximately 20-nm-thick MuM flake. Fitting of the experimental data to the hopping-conduction (HC) model indicates an increase in the conduction-band (CB) carrier density with the reduction in the number of layers. Further, layer-dependent work-function measurements suggest a shift in the Fermi level toward the CB for reduced thickness, thus confirming the doping effects. This increase in the carrier density with the reduction in the number of layers may be due to surface doping and lattice relaxation. These results show the possibility of using few-layer mica as a layered wide-band-gap semiconductor for 2D electronic devices.

II. EXPERIMENTS

Commercially available MuM substrates are mechanically exfoliated and transferred onto 300-nm SiO_2/Si substrates. After transfer, samples are rinsed in acetone and isopropanol to remove any residue, followed by a dehydration bake on a hot plate at 120 °C for 5 min. The flakes are identified using an optical microscope and their thickness is measured using a Park NX10 atomic force microscope. Raman-spectroscopy measurements are performed using a confocal Raman microscope in backscattering geometry with a 100× objective and a 2.54-eV continuous-wave laser as the excitation source. For electrical measurements, the contact electrodes are defined as being approximately 1 μm apart using standard electron-beam lithography followed by electron-beam evaporation of Ni/Au (30 nm/30 nm). The deposited metal is uniform and conformal, which is sufficient to give good contact with flakes of thickness approximately 100 nm. All the electrical measurements are carried out in the dark at room temperature using a Cascade Microtech Summit 12000AP probe station and an Agilent B1500A Semiconductor Parameter Analyzer in high-resolution mode (HR-SMU), with a resolution of 10 fA. Thickness-dependent work-function measurements are performed using a Shimandu SPM8000-FM scanning probe microscope at ambient conditions.

III. RESULTS AND DISCUSSION

The MuM flakes on SiO_2/Si, identified optically, are $\geq$10 nm—that is, $\geq$5 layers—due to the large cleavage energy [7] and the poor optical contrast on 300-nm SiO_2/Si substrate [22]. The optical contrast is better on thin oxide substrates; however, due to the large leakage current through the substrate, 300-nm oxide substrates are used for all the electrical measurements. Raman spectra of MuM before and after the exfoliation are measured (not shown here). The Raman spectrum of bulk MuM (approximately 100 μm) shows all the characteristic peaks [36]; however, no Raman modes are observed in flakes with thickness $<$100 nm. Therefore, the Raman spectrum could not be used as a tool to identify the number of layers in MuM flakes. The Raman-scattering cross section of MuM flakes may be increased under resonant conditions; however, it has not been analyzed in this work.

For electrical characterization, three different MuM flakes on SiO_2/Si with thicknesses of approximately 100 nm (T_1), approximately 20 nm (T_2), and approximately 10 nm (T_3) are selected: optical images are shown in Figs. 2(a)–2(c). For the initial studies, devices with two electrical contacts are fabricated with an electrode separation of 1 μm. The Si substrate is used as the back gate to apply the gate bias voltage (V_{bias}). The measured gate leakage currents are at least 2 orders of magnitude lower than the in-plane current and show no response to increased bias voltages, indicating that there is negligible branching of current to the substrate contact. The measured two-probe I-V characteristics of these three devices are shown in Figs. 2(d)–2(f). For comparison, the y axes are shown in terms of the current density (J) in A cm^{-2}. The current in device T_1 is almost linear and below 0.5 pA (5×10^{-4} A cm^{-2}) for the entire range of the applied voltage (V_{in}), whereas the devices T_2 and T_3 show an exponential behavior with V_{in}. Also, the current in T_3 is almost 3 orders of magnitude larger than that in T_2. Figure 2(g) shows the I-V plot of three measurements on each of the indicated devices. The thickness-dependent I-V characteristics of the MuM flakes are found to be repeatable over different measurement cycles as well as for different devices within the experimental limits. This also indicates that the observed current is not due to dielectric breakdown or any such permanent damage to the MuM flakes. As a reference, a device with exactly the same structure but with no MuM flake is also characterized: the plot is shown as the black curve. Devices T_2 and T_3 are further characterized for the effect of V_{bias}: the results are as shown in Fig. 2(h). It is observed that the current through the MuM flakes decreases for both positive and negative V_{bias}. This indicates that the effect of the gate bias on MuM flakes is not dominated by conventional field-effect channel formation, i.e., the applied V_{bias} results in neither accumulation nor inversion. Instead, the in-plane mobility of the carriers is reduced due to the applied out-of-plane electric field, resulting in a decrease of the in-plane current. Further, this degradation effect is more pronounced for thinner flakes (T_3) when compared to the thicker ones (T_2), as observed in previous reports

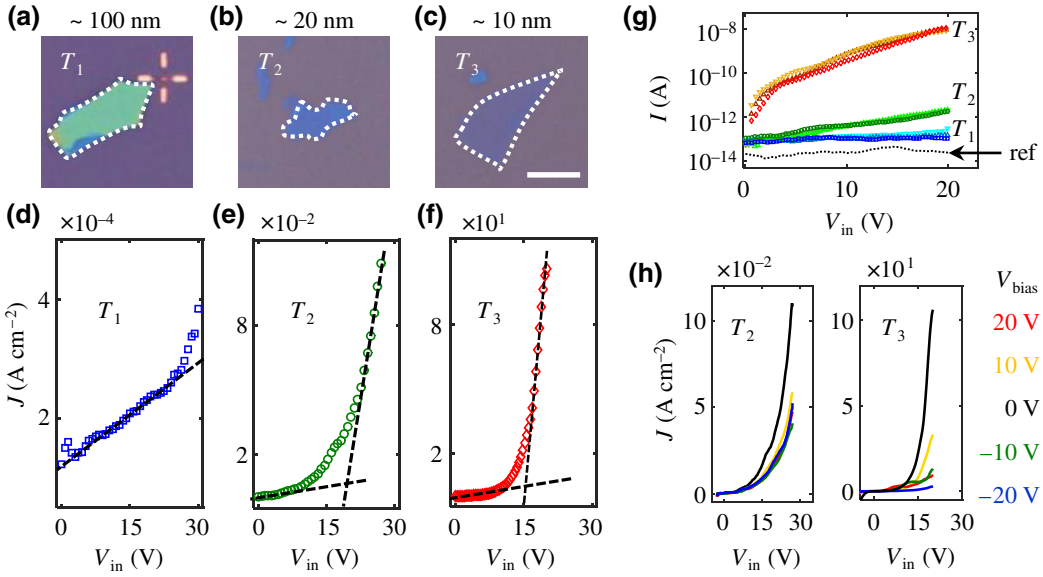

FIG. 2. Two-probe measurements. (a)–(c) Optical images and (d)–(f) the corresponding I-V characteristics of MuM/SiO_2/Si with thickness $T_1 \sim 100$ nm, $T_2 \sim 20$ nm, and $T_3 \sim 10$ nm. The scale bar shown in (c) is 5 μm and the y axis is shown in terms of the current density (J) in A cm^{-2}. (g) The I-V characteristics for three measurements on each of the devices, T_1, T_2, and T_3, with $V_{bias} = 0$ V. The black curve marked as "ref" corresponds to the I-V plot of SiO_2/Si, i.e., without an MuM flake under similar device and measurement configurations. (h) The effect of V_{bias} on the I-V characteristics of Mu/SiO_2/Si for T_2 and T_3 for the applied V_{bias} as listed.

[37,38]. For instance, at $V_{\text{bias}} = -20$ V and $V_{\text{in}} = 15$ V, the current through the T_3 (T_2) flake is 0.04 (0.54) times the current at zero bias. These effects can mainly be attributed to the field-dependent intrinsic electron-phonon scattering in mica flakes [39]. Due to the out-of-plane electric field, the carriers are pushed to either side, thereby reducing the effective channel thickness and increasing the phonon scattering [39]. Another component adding to the mobility degradation can be attributed to the MuM-SiO_2 interface phonon scattering [40,41]. Any scattering effects due to the interface charge impurities, oxide traps, or substrate roughness can be neglected, as they show asymmetric behavior with the applied gate bias voltages [41,42]. The exact mechanism of this mobility degradation does, however, call for further experimentation.

In order to account for the contact resistance and its dependence on the MuM flake thickness, four-probe devices of MuM flake thickness corresponding to T_2 and T_3 are fabricated. Figure 3(a) shows the measurement schematic along with the optical image of one of the fabricated four-probe devices. The devices are fabricated on flakes of appropriate shapes to ensure correct geometry of the linear four-probe electrodes. The fabricated electrodes are 1 μm × 5 μm in area, with an electrode-to-electrode separation of 1 μm. For the four-probe measurements, the current is applied between the contacts marked "1" and "4," whereas for the two-probe measurements it is applied between the contacts marked "2" and "3." The voltage is measured between the contacts marked "2" and "3." The currents applied to T_2 (T_3) are in the range 0–10 pA (0–10 nA), determined from the results shown in Fig. 2. The mean and standard deviation in the measured voltage of six different readings obtained from the four-probe and two-probe I-V characteristics are as shown in Fig. 3(b). The two I-V characteristics are almost the same, but the mean measured voltage around the 5-nA current in the four-probe measurements is slightly less than that in the two-probe measurements. However, due to large resistance of the MuM flakes, of the order of 10^{12} Ω (10^9 Ω) in T_2 (T_3), with approximately 10% standard deviation, the contact resistance cannot be estimated in these devices. The obtained I-V characteristics of these devices is independent of the direction of the applied current, as shown in Fig. 3(c). The conductivity of the MuM flakes, estimated from the slope of the four-probe I-V characteristics around 10 V, is approximately 0.8 μS cm^{-1} for T_2, whereas it is approximately 0.4 mS cm^{-1} for T_3, 3 orders of magnitude larger than for T_2. To further understand the behavior of devices T_2 and T_3, the experimental four-probe I-V data are compared to different conduction models. Earlier reports on conduction in micas have shown that there is a negligible effect of different metal contacts [31,32] and in the present case, the possibility of tunneling is negligible. Therefore, the devices are initially compared with the Poole-Frenkel (PF) model, as given by Eq. (1), to extract the material parameters [32]:

$$J/E = q\mu N_c \left(\frac{N_d}{N_t}\right)^{1/2} \exp\left(C_1\sqrt{E} - \frac{q\Phi_t}{kT}\right), \quad (1)$$

where q is the electronic charge, μ is the carrier mobility, k is the Boltzmann constant, T is the absolute temperature, $q\Phi_t$ is the trap energy level, and N_C, N_d, and N_t are, respectively, the density of the CB, the defect, and the trap states. There exists a linear relation $\ln(J/E) = C_1\sqrt{E} + \ln C_o$, where all the constant terms are absorbed in C_o and the slope C_1 is given by Eq. (2), where ϵ_o and ϵ_r are, respectively, the free-space and relative optical permittivity of the material:

$$\text{Slope } C_1 = \sqrt{\frac{q^3}{\pi\epsilon_o\epsilon_r kT}}. \quad (2)$$

Figure 3(d) shows $\ln(J/E)$ versus $\sqrt{E}$, also known as the PF plot, for the experimentally obtained data of devices T_2 and T_3, shown in green and red, respectively, along with the linear fit to the PF model, shown in black. The best linear fit for T_2 (T_3) is obtained for the applied current ≥6 pA (≥1 nA), with the reduced R^2 0.96 (0.98) and the rms error 0.03 (0.04) as the fitting parameters. The slope C_1 in the units of (cm/MV)$^{1/2}$ extracted from the linear fit for T_2 (T_3) are 12.23 (18.03). These values of C_1 are used in Eq. (2) and further in Eq. (1) to obtain an exponential fit (not shown) and extract the material parameters, as listed in Table I. It is observed that ϵ_r for T_2 (T_3) is 5.74 (2.65), which is less than the low-frequency permittivity of mica (approximately 7.1) but larger than the optical value (approximately 2.5), indicating that the transit time of the carriers is larger than the dielectric relaxation time of the material. Also, assuming that $(N_d/N_t)^{1/2} = 10^{-2}$, the product μN_c is exceptionally small in both cases [32], indicating low carrier mobility. These observations suggest that the PF is not the dominant conduction mechanism.

Next, the possibility of the HC model is considered for analysis using the $J - E$ relation given by Eq. (3), where L_h is the mean hopping distance, n is the CB carrier density, ν is the thermal vibration frequency of the electron at the trap site, and ε_h is the hopping energy, i.e., the energy between the trap level and the edge of the CB:

$$J = (qL_h n\nu)\exp\left(K_1 E - \frac{\varepsilon_h}{kT}\right). \quad (3)$$

There exists a linear relation $\ln(J) = K_1 E + \ln K_o$, where all the constant terms are absorbed in K_o and the slope K_1 is given by Eq. (4), where symbols have meanings as defined

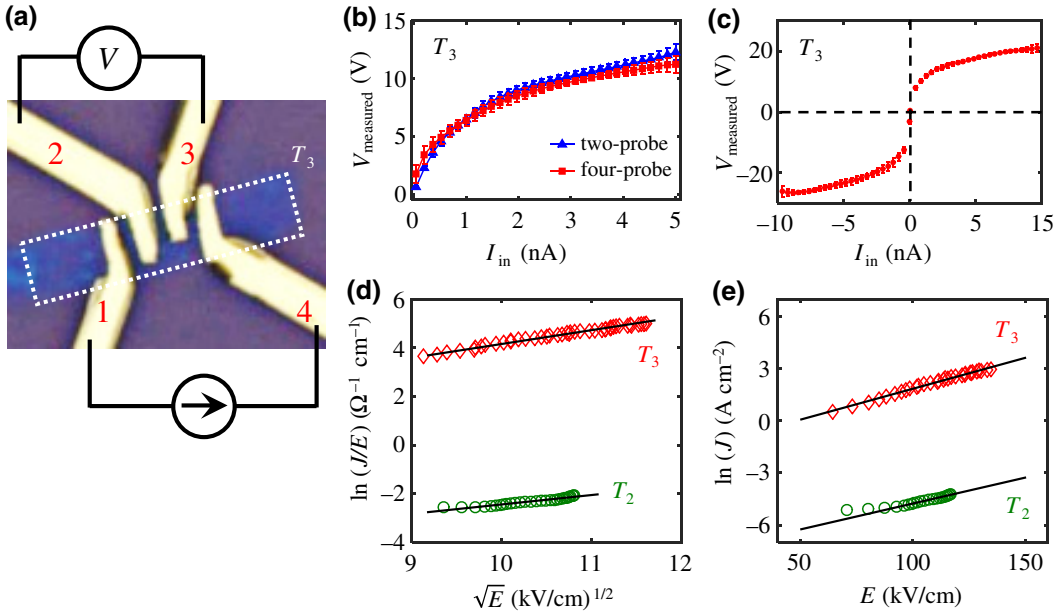

FIG. 3. Four-probe measurements. (a) A schematic of the four-probe conductivity measurement setup with the optical image of a fabricated device. (b) The mean and standard deviation in the measured voltage of six different readings of the two-probe and four-probe measurements on the device shown in (a). (c) The forward and backward four-probe I-V characteristics of the device shown in (a). (d) A Poole-Frenkel plot showing the natural log of J/E in Ω^{-1} cm^{-1} versus the square root of the electric field E in kV/cm for T_2 shown in green and T_3 shown in red, along with their fit to Eq. (1) shown using a black line. (e) A hopping-conduction plot showing the natural log of the current density J in A cm^{-1} versus the electric field E in kV/cm for T_2 shown in green and T_3 shown in red, along with their fit to Eq. (3) shown using a black line.

earlier:

$$\text{Slope } K_1 = \frac{qL_h}{kT} \text{ (cm/V)}. \tag{4}$$

Figure 3(e) shows ln(J) versus E, the HC plot for the experimentally obtained data of devices T_2 and T_3, shown in green and red, respectively, along with the linear fit to the HC model, shown in black. The best linear fit for T_2 (T_3) is obtained for the applied current ≥6 pA (≥0.5 nA), with the reduced R^2 0.99 (0.99) and the rms error 0.02 (0.06) as the fitting parameters. The extracted slopes K_1 in (cm/MV) for T_2 (T_3) are 27.84 (35.59). These values of K_1 are used in Eq. (4) and further in Eq. (3) to obtain the exponential fit (not shown) and extract the material parameters,

TABLE I. Material parameters extracted from the fitting of the indicated conduction model.

Poole-Frenkel model	ϵ_r	Φ_t (V)	μN_C (V s cm)$^{-1}$
Sample T_2	5.74	0.18	1.1×10^{15}
Sample T_3	2.65	0.18	1.61×10^{17}
Hopping-conduction model	L_h (mn)	ε_h (eV)	n (cm^{-3})
Sample T_2	7.2	0.20	1.03×10^{12}
Sample T_3	9.2	0.20	4.05×10^{14}

as listed in Table I. For all the calculations, ν is assumed to be 10^{13} Hz [32]. It is observed that the mean hopping length (L_h) for T_2 is approximately 7.2 nm, whereas for T_3 it is approximately 9.2 nm. The CB carrier density (n) in T_2 is 1.03×10^{12}, whereas in T_3 it is 4.05×10^{14}, approximately 400 times larger than that in T_2.

To investigate the increase in n for a reduced thickness as indicated by the model-based analysis, the thickness-dependent work function of the MuM flakes (φ) is measured using Kelvin probe force microscopy for a MuM flake on Si substrate as shown in Fig. 4(c). The measured thickness profile and the corresponding contact potential difference (CPD) along the lines indicated in Fig. 4(c) are shown in Figs. 4(a) and 4(b), respectively. The work function φ is calculated using the relation CPD $= (\varphi - \varphi_t)/q$ at 25 different points over the scanned region, where φ_t is the work function of the Pt-Ir tip (4.9 eV). The 99.7% confidence bound (4σ) of the error in φ is found to be ≤ 0.03 eV. The calculated φ in electronvolts as a function of the flake thickness, shown in Fig. 4(d), shows a decrease in the mean value of φ from 5.09 eV to 4.93 eV for a decrease in MuM flake thickness from 21 nm to 14 nm. Assuming that the measured φ corresponds to the Fermi level (ε_F), there is an upward movement of ε_F toward the CB with the reduction in thickness, indicating an increase in the CB carrier density (n), which is

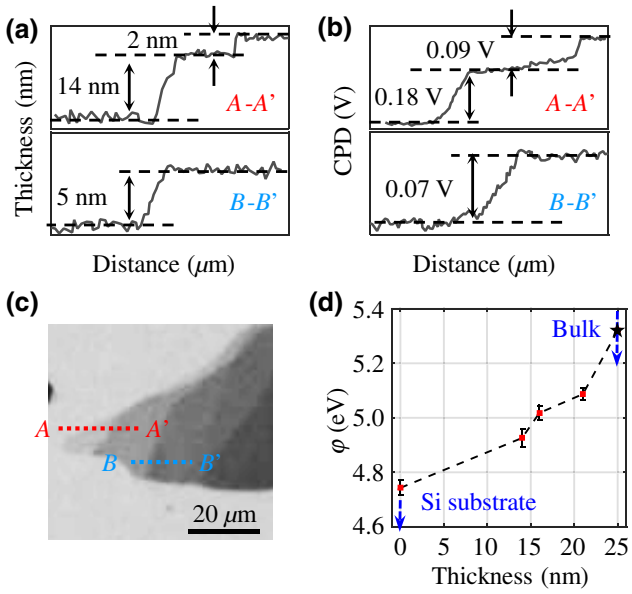

FIG. 4. (a) The thickness profiles and (b) the corresponding contact potential difference (CPD) of a muscovite flake, with an optical image as shown in (c), along sections A-A' and B-B'. All the measurements are carried out at ambient conditions using a Pt-Ir tip, maintained at 0 V. (d) The obtained work function φ in electronvolts for different flake thicknesses, where zero thickness corresponds to the Si substrate, while the point marked as bulk at 5.32 eV corresponds to the surface potential of a 40-μm-thick flake reported earlier [43]. The Pt-Ir tip work function φ_t is taken to be 4.9 eV.

also indicated from electrical measurements (as given in Table I). For comparison, the change in n due to the shift in the Fermi level ($\Delta\varepsilon_F$) can be estimated using the relation $n = N_C \exp\{-[(E_C - \varepsilon_F)/kT]\}$ under the Boltzmann approximation, where N_C is the effective density of states in the CB and E_C is the CB minimum [44]. The change in n with the reduction in flake thickness and hence $\Delta\varepsilon_F$ can be given as $\exp(\Delta\varepsilon_F/kT)$. Since only the shift $\Delta\varepsilon_F$ relative to E_C has been considered here for the calculations, any complexities in the band structure can be neglected [44]. For a shift in the mean of ε_F by 0.16 eV, the increase in n is approximately 470, which is of the same order of magnitude as extracted from the HC-model fitting of the measured I-V data.

This increase in the conductivity due to the increased carrier density cannot be due to structure change from crystalline to an amorphous phase, as MuM is known to retain its crystal structure even in the monolayer limit [45,46]. The tetrahedral layers in MuM, as discussed earlier, have excess electrons due to trivalent substitution, the mobility of which may increase due to lattice relaxation [33]. Further, it has earlier been shown computationally that, when compared to bulk, there is an increased contribution from surface K^+ ions near the CB edge in monolayer MuM [35]. Both of these effects are thickness dependent and are supposed to be dominant in the monolayer limit. Therefore, the observed increase in the device current for T_3 (approximately five layers) when compared to T_2 (approximately ten layers) may be attributed to the surface doping due to the increased contribution from the K^+ ions and lattice relaxation. However, the exact mechanism will require further experiments.

IV. CONCLUSION

In conclusion, we observe an increased in-plane nonlinear conductivity in few-layer muscovite mica (MuM) flakes. Comparison with the HC model indicates an increase in the CB carrier density for a reduced thickness. This is corroborated by the work-function measurements. The observed effect is attributed to the increase in the surface doping and lattice relaxation. This preliminary study shows that there is a possibility of using mica as a wide-band-gap semiconductor and that it can open up avenues for 2D electronic devices.

ACKNOWLEDGMENTS

This work was supported in part by the Department of Science and Technology, Government of India (DST-GoI), which lead to the establishment of the Nano Functional Materials Technology Centre (NFMTC) (Grants No. SR/NM/NAT/02-2005 and No. DST/NM/JIIT-01/2016(C)), in part by the Japan Student Services Organization for the advanced Project Based Learning (aPBL), and in part by the Shibaura Institute of Technology under the Top Global University Project, designed by the Ministry of Education, Culture, Sports, Science and Technology in Japan. A.A. would like to thank Mr. Nirjhar Kumar for fruit-full discussions. K.L.G. acknowledges the financial support from the DST-GoI, with Sanction Order No. DST/INSPIRE/04/2016/001865 under the DST "Innovation in Science Pursuit for Inspired Research" (INSPIRE) Faculty program.

[1] D. Jariwala, V. K. Sangwan, L. J. Lauhon, T. J. Marks, and M. C. Hersam, Emerging device applications for semiconducting two-dimensional transition metal dichalcogenides, ACS Nano **8**, 1102 (2014).

[2] G. Fiori, F. Bonaccorso, G. Iannaccone, T. Palacios, D. Neumaier, A. Seabaugh, S. K. Banerjee, and L. Colombo, Electronics based on two-dimensional materials, Nat. Nanotechnol. **9**, 768 (2014).

[3] X. Wang, Y. Sun, and K. Liu, Chemical and structural stability of 2D layered materials, 2D Mater. **6**, 042001 (2019).

[4] R. Frisenda, Y. Niu, P. Gant, M. Muñoz, and A. Castellanos-Gomez, Naturally occurring van der Waals materials, npj 2D Mater. Appl. **4**, 1 (2020).

[5] D. M. Hepburn, I. J. Kemp, and A. J. Shields, Mica, IEEE Electr. Insul. Mag. **16**, 19 (2000).

[6] L. Pauling, The structure of the micas and related minerals, Proc. Natl. Acad. Sci. USA **16**, 123 (1930).

[7] J. Obreimoff, The splitting strength of mica, Proc. R. Soc. London A **127**, 290 (1930).

[8] J. H. Jung, C.-H. Park, and J. Ihm, A rigorous method of calculating exfoliation energies from first principles, Nano Lett. **18**, 2759 (2018).

[9] W. de Poel, S. Pintea, J. Drnec, F. Carla, R. Felici, P. Mulder, J. A. Elemans, W. J. van Enckevort, A. E. Rowan, and E. Vlieg, Muscovite mica: Flatter than a pancake, Surf. Sci. **619**, 19 (2014).

[10] X. Lu, L. Majewski, and A. Song, Electrical characterization of mica as an insulator for organic field-effect transistors, Org. Electron. **9**, 473 (2008).

[11] J. Feenstra, M. Van Eerden, A. K. Lemmens, W. De Poel, P. H. Kouwer, A. E. Rowan, and J. J. Schermer, Muscovite mica as a growth template of PC 61 BM crystallites for organic photovoltaics, CrystEngComm **19**, 4424 (2017).

[12] Y. Bitla and Y.-H. Chu, Micatronics: A new platform for flexible X-tronics, FlatChem **3**, 26 (2017).

[13] M. Yen, Y. Bitla, and Y.-H. Chu, Van der Waals heteroepitaxy on muscovite, Mater. Chem. Phys. **234**, 185 (2019).

[14] Q. Ji, Y. Zhang, T. Gao, Y. Zhang, D. Ma, M. Liu, Y. Chen, X. Qiao, P.-H. Tan, M. Kan, *et al.*, Epitaxial monolayer MoS_2 on mica with novel photoluminescence, Nano Lett. **13**, 3870 (2013).

[15] A. Castellanos-Gomez, M. Wojtaszek, N. Tombros, N. Agraït, B. J. van Wees, and G. Rubio-Bollinger, Atomically thin mica flakes and their application as ultrathin insulating substrates for graphene, Small **7**, 2491 (2011).

[16] J. Shim, C. H. Lui, T. Y. Ko, Y.-J. Yu, P. Kim, T. F. Heinz, and S. Ryu, Water-gated charge doping of graphene induced by mica substrates, Nano Lett. **12**, 648 (2012).

[17] Z. Ben Aziza, Q. Zhang, and D. Baillargeat, Graphene/mica based ammonia gas sensors, Appl. Phys. Lett. **105**, 254102 (2014).

[18] J. Mohrmann, K. Watanabe, T. Taniguchi, and R. Danneau, Persistent hysteresis in graphene-mica van der Waals heterostructures, Nanotechnology **26**, 015202 (2014).

[19] X. Zhang, Y. He, R. Li, H. Dong, and W. Hu, 2D mica crystal as electret in organic field-effect transistors for multistate memory, Adv. Mater. **28**, 3755 (2016).

[20] W. G. Lim, D. U. Lee, H. G. Na, H. W. Kim, and T. W. Kim, Electrical bistabilities and memory mechanisms of nonvolatile organic bistable devices based on exfoliated muscovite-type mica nanoparticle/poly (methylmethacrylate) nanocomposites, Appl. Surf. Sci. **432**, 228 (2018).

[21] H. Lin, J. D. Cojal Gonzàlez, N. Severin, I. M. Sokolov, and J. P. Rabe, Reversible switching of charge transfer at the graphene-mica interface with intercalating molecules, ACS Nano **14**, 11594 (2020).

[22] C. G. Low and Q. Zhang, Ultra-thin and flat mica as gate dielectric layers, Small **8**, 2178 (2012).

[23] C. G. Low, Q. Zhang, Y. Hao, and R. S. Ruoff, Graphene field effect transistors with mica as gate dielectric layers, Small **10**, 4213 (2014).

[24] K. Xu, P. Cao, and J. R. Heath, Graphene visualizes the first water adlayers on mica at ambient conditions, Science **329**, 1188 (2010).

[25] A. Rudenko, F. Keil, M. Katsnelson, and A. Lichtenstein, Graphene adhesion on mica: Role of surface morphology, Phys. Rev. B **83**, 045409 (2011).

[26] O. Ochedowski, B. K. Bussmann, and M. Schleberger, Graphene on mica-intercalated water trapped for life, Sci. Rep. **4**, 1 (2014).

[27] P. Bampoulis, K. Sotthewes, M. H. Siekman, H. J. Zandvliet, and B. Poelsema, Graphene visualizes the ion distribution on air-cleaved mica, Sci. Rep. **7**, 1 (2017).

[28] L. Mogg, G.-P. Hao, S. Zhang, C. Bacaksiz, Y.-C. Zou, S. Haigh, F. Peeters, A. Geim, and M. Lozada-Hidalgo, Atomically thin micas as proton-conducting membranes, Nat. Nanotechnol. **14**, 962 (2019).

[29] A. von Hippel, Electronic conduction in insulating crystals under very high field strength, Phys. Rev. **54**, 1096 (1938).

[30] M. McColl, Ph.D. thesis, California Institute of Technology (1964), https://thesis.library.caltech.edu/4081/.

[31] A. Davidson and A. Yoffe, Hopping electrical conduction and thermal breakdown in natural and synthetic mica, Phys. Stat. Sol. B **30**, 741 (1968).

[32] H. Baessler, G. Basel, G. Berg, S. Egle, and N. Riehl, Electron transport through mica, Phys. Stat. Sol. A **4**, 701 (1971).

[33] H. Lindgreen, Electrical conduction in layer silicates investigated by combined scanning tunnelling microscopy and atomic force microscopy, Clay. Miner. **35**, 643 (2000).

[34] V. Saltas, D. Pentari, and F. Vallianatos, Complex electrical conductivity of biotite and muscovite micas at elevated temperatures: A comparative study, Materials **13**, 3513 (2020).

[35] S. S. Kim, T. V. Khai, V. Kulish, Y.-H. Kim, H. G. Na, A. Katoch, M. Osada, P. Wu, and H. W. Kim, Tunable bandgap narrowing induced by controlled molecular thickness in 2D mica nanosheets, Chem. Mater. **27**, 4222 (2015).

[36] D. A. McKeown, M. I. Bell, and E. S. Etz, Vibrational analysis of the dioctahedral mica: 2M1 muscovite, Am. Mineral. **84**, 1041 (1999).

[37] M. Mottaghi and G. Horowitz, Field-induced mobility degradation in pentacene thin-film transistors, Org. Electron. **7**, 528 (2006).

[38] S.-L. Li, K. Wakabayashi, Y. Xu, S. Nakaharai, K. Komatsu, W.-W. Li, Y.-F. Lin, A. Aparecido-Ferreira, and K. Tsukagoshi, Thickness-dependent interfacial coulomb scattering in atomically thin field-effect transistors, Nano Lett. **13**, 3546 (2013).

[39] D. Ahn and S. Chuang, Electric field dependence of intrasubband polar-optical-phonon scattering in a quantum well, Phys. Rev. B **37**, 2529 (1988).

[40] K. Hess and P. Vogl, Remote polar phonon scattering in silicon inversion layers, Solid. State. Commun. **30**, 797 (1979).

[41] S. Bhattacharjee, K. L. Ganapathi, H. Chandrasekar, T. Paul, S. Mohan, A. Ghosh, S. Raghavan, and N. Bhat, Nitride dielectric environments to suppress surface optical phonon dominated scattering in high-performance multilayer MoS_2 FETs, Adv. Electron. Mater. **3**, 1600358 (2017).

[42] M. Gurfinkel, H. D. Xiong, K. P. Cheung, J. S. Suehle, J. B. Bernstein, Y. Shapira, A. J. Lelis, D. Habersat, and N. Goldsman, Characterization of transient gate oxide trapping in SiC MOSFETs using fast *I–V* techniques, IEEE Trans. Electron Devices **55**, 2004 (2008).

[43] Y. Hashimoto and T. Sakakibara, Effect of surface current on photoelectron emission from mica, Electr. Eng. Jpn. **133**, 1 (2000).

[44] M. Siao, W. Shen, R. Chen, Z. Chang, M. Shih, Y. Chiu, and C.-M. Cheng, Two-dimensional electronic transport and surface electron accumulation in MoS_2, Nat. Commun. **9**, 1 (2018).

[45] A. Castellanos-Gomez, M. Poot, A. Amor-Amorós, G. A. Steele, H. S. van der Zant, N. Agraït, and G. Rubio-Bollinger, Mechanical properties of freely suspended atomically thin dielectric layers of mica, Nano Res. **5**, 550 (2012).

[46] F. Jia and S. Song, Preparation of monolayer muscovite through exfoliation of natural muscovite, RSC Adv. **5**, 52882 (2015).